




Phase diagram with an antiferroelectric/ferroelectric phase boundary in $\text{AgNbO}_3\text{-LiTaO}_3$ energy-storage ceramics by lattice dynamics and electronic transitions

Kai Dai (戴凯),¹ Anyang Cui (崔安阳) ^{1,*} Yan Ye (叶艳),¹ Kai Jiang (姜凯),¹ Jinzhong Zhang (张金中),¹ Yawei Li (李亚巍) ¹ Genshui Wang (王根水),² Xianlin Dong (董显林),² Zhigao Hu (胡志高) ^{1,3,4,†} and Junhao Chu (褚君浩)^{1,3,4}

¹Technical Center for Multifunctional Magneto-Optical Spectroscopy (Shanghai), Engineering Research Center of Nanophotonics & Advanced Instrument (Ministry of Education), Department of Materials, School of Physics and Electronic Science, East China Normal University, Shanghai 200241, China

²Key Laboratory of Inorganic Functional Materials and Devices, Shanghai Institute of Ceramics, Chinese Academy of Sciences, Shanghai 200050, China

³Collaborative Innovation Center of Extreme Optics, Shanxi University, Taiyuan, Shanxi 030006, China

⁴Shanghai Institute of Intelligent Electronics & Systems, Fudan University, Shanghai 200433, China



(Received 22 June 2021; revised 16 September 2021; accepted 25 October 2021; published 4 November 2021)

Here, a phase diagram with phase coexistence near the polycrystalline phase boundary has been studied on $(1-x)\text{AgNbO}_3\text{-}x\text{LiTaO}_3$ ceramics by analyzing infrared- (IR) and Raman-active phonon dynamics under tuning chemical component and temperature. Optical dielectric functions, ferroelectric domain, and electronic transitions promote the understanding of lattice structure in AgNbO_3 , and the antiferroelectric (AFE) to ferroelectric (FE) transformation, which results from the joint effect of the cationic antipolar and the oxygen octahedron distortion. The spectroscopic methods of x-ray diffraction, IR reflection, and Raman scattering reveal the mixed phase boundary at $x(\text{LiTaO}_3) = 0.05$, which is the indication of a first-order transition, contributing to the excellent pyroelectric property. Note that the soft mode near 50 cm^{-1} is sensitive to reveal the lattice transformation. Moreover, the temperature-dependent optical band gap (E_g) with the specific electronic transition behavior has been further explored, and becomes complementary evidence for the structural phase transition. This study presents the systematical results on structural properties and optical/dielectric properties for the state-of-the-art AgNbO_3 system for designing energy-storage devices.

DOI: [10.1103/PhysRevB.104.174104](https://doi.org/10.1103/PhysRevB.104.174104)

I. INTRODUCTION

Lead-free ceramics are of increasing interest for exploring the industrial pyroelectric and energy-harvesting devices with high-performance environment-friendly requirements. To take the place of the commercial $\text{Pb}(\text{Zr,Ti})\text{O}_3$ -based oxides with the toxic components [1,2], it is urgent to seek an ideal lead-free candidate with comparable performance [3–5]. Recently, AgNbO_3 -based antiferroelectric (AFE) ceramic was confirmed to hold the promising dielectric, pyroelectric, and energy-storage characteristics due to its AFE-like hysteresis loops with high saturation polarization [6–9]. Francombe *et al.* first studied the basic structure and the common functionalities of AgNbO_3 [10]. A successive phase transition was then observed on AgNbO_3 [11]: $M_1 \xrightarrow{340\text{ K}} M_2 \xrightarrow{540\text{ K}} M_3 \xrightarrow{626\text{ K}} O_1 \xrightarrow{634\text{ K}} O_2 \xrightarrow{660\text{ K}} T \xrightarrow{852\text{ K}} C$. High-temperature T-C, O-T, and M_3 -O transitions are considered to be induced by the tilt of the oxygen octahedron, revealed by the series of x-ray diffraction (XRD), transmission electron microscopy, and dielectric spectra [12]. Structure transitions among M_1 , M_2 , and M_3 phases are related to the displacement of Ag^+ or Nb^{5+} ions [13,14], where both O, T, and C phases belong

to the paraelectric (PE) phase, the M_2 and M_3 phases belong to the disordered AFE phase, and M_1 is the AFE-dominated ferroelectric (FIE) phase, respectively.

Between the initial AFE phase (pure AgNbO_3) and the induced ferroelectric (FE) one, the free energy difference reaches a large level to prevent the transition among the adjacent phases. Fortunately, chemical modification could effectively reduce the gap of free energy at the AFE state, and consequently achieve the AFE-FE transition under a low electric field. It is found that chemical modification for AgNbO_3 can contribute to induce the FE phase by replacing cations, such as Li^+ [15,16] and K^+ [7,17,18]. The substitution of Li^+ could make the AgNbO_3 -based lattice change from orthorhombic to rhombohedral (*R*) phase [19], where the *R* phase is inherently derived from the ionic displacement of Ag/Li, Nb, and O. On the other hand, Valant and Zhao *et al.* obtained high-quality $\text{Ag}(\text{Nb}_{1-x}\text{Ta}_x)\text{O}_3$ ceramics with enhanced permittivity and energy-storage density by the attempt of Ta^{5+} modification [9,20–22]. Therefore, LiTaO_3 -doping AgNbO_3 ceramics show the improved performance with a large pyroelectric coefficient ($3.68 \times 10^{-8}\text{ C cm}^{-2}\text{ K}^{-1}$) at room temperature, and the giant pyroelectric energy density (1.4 J cm^{-3}) for the composition of $x = 0.05$ [23], which may be caused by the AFE/FE (nonpolar and polar) phase boundary. However, the systematic study on the fundamental phase diagram, soft mode characteristic, and

*aycui@phy.ecnu.edu.cn

†zghu@ee.ecnu.edu.cn

optical transition behaviors of the AgNbO_3 system is absent. Infrared (IR) and Raman scattering spectroscopies are complementary and highly sensitive to small distortions of the structural (ferroelectric-paraelectric phase) or nonstructural (ferromagnetic-paramagnetic phase) transition on a molecular scale [24–29]. Simultaneously, spectroscopic ellipsometry (SE) could determine the dielectric functions and optical transition behaviors of the ceramics [30,31]. These condensed matter spectroscopic methods can provide many significant physical evidences on the structure property, such as phonon and soft mode behavior [32,33], dielectric function, optical transition, and so on.

We employ XRD, molecular-scale IR and Raman spectra, piezoresponse force microscopy (PFM), and SE characterizations to systematically investigate the dopant and temperature-dependent phonon dynamics, lattice symmetry, ferroelectric domain, electronic transition, and phase transformation of $(1-x)\text{AgNbO}_3-x\text{LiTaO}_3$ (ANLT) ceramics. The IR-active and Raman-active phonon behaviors at the identified M_1 and R phases of ANLT ceramics have been summarized with different compositions. Correspondingly, the ionic substitution of Li/Ta would make AgNbO_3 ceramics change from AFE to FE phase, and appear in the mediate phase coexistence at $x = 0.05$. In addition, temperature effects on the dielectric function and electronic transition of ANLT ceramics have been explored as complementary evidence. Eventually, a complete phase transition ordering [$M_1/R-M_2-M_3-O-T$] has been accurately depicted. The phase boundary region with coexisted symmetry groups observed in our work would strengthen the fundamental understanding for the excellent pyroelectric performances in the AgNbO_3 -based system.

II. MATERIALS AND METHODS

$(1-x)\text{AgNbO}_3-x\text{LiTaO}_3$ ceramics were prepared by the solid-state reaction method. The sample preparation process can be referred to in the literature [23]. Samples of $x = 0.04, 0.05, 0.07,$ and 0.10 are noted as ANLT04, ANLT05, ANLT07, and ANLT10, respectively.

Structures of ANLT were analyzed by XRD (Japan Smart-Lab), with a $\text{Cu K}\alpha$ rotating source. IR reflection spectra were implemented by a Bruker Vertex 80 V Fourier transform infrared spectrometer (Bruker Co., Billerica, MA) equipped with a specular reflection device at the range of $50\text{--}1000\text{ cm}^{-1}$ and the incident angle of 6° . A gold mirror was utilized as an internal reference due to its absolute reflectance. Raman scattering was achieved on a micro-Raman spectrometer (Jobin-Yvon LabRAM HR 800 UV) with the frequency range of $5\text{--}1000\text{ cm}^{-1}$, $\lambda_{\text{excited}} = 532\text{ nm}$, and spectral resolution of better than 1 cm^{-1} . Linkam THMSE 600 heating/cooling stage was equipped for the temperature-dependent experiment at $80\text{--}800\text{ K}$. The heating/cooling rate was 10 K/min and accurate to $\pm 0.1\text{ K}$. To facilitate the spectral comparison at wide temperature ranges and eliminate the temperature effect, all scattering spectra are corrected by the Bose-Einstein factor coefficient [34] $n(\omega, T) = [\exp(\hbar\omega/kT) - 1]^{-1}$, where \hbar , ω , k , and T represent Planck's constant, phonon wave number, Boltzmann constant, and temperature, respectively.

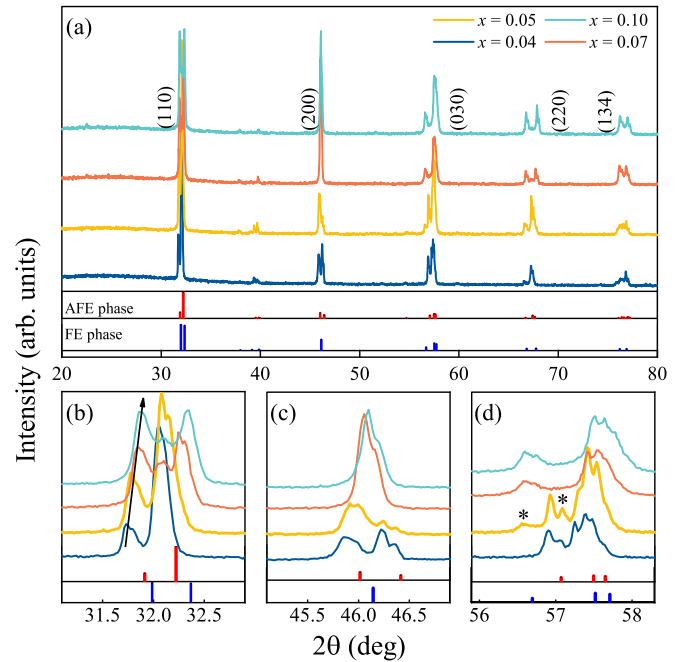


FIG. 1. (a) XRD patterns and (b)–(d) the enlarged XRD patterns of the ANLT ceramics.

The fundamental principle of SE aims to determine the complex dielectric function by quantifying the change of amplitude and phase of the reflected light from the sample surface and interface. SE measurements were performed on a visible-ultraviolet spectroscopic ellipsometer in the photon energy range of $1.55\text{--}4.96\text{ eV}$ ($800\text{--}250\text{ nm}$) (V-VASE by J. A. Woolam Co., Inc.) with the spectral resolution of 5 nm . The incident angle was fixed at 70° . An Instec cell with a liquid nitrogen cooling accessory was employed with the temperature range from 200 to 500 K , and a temperature accuracy of $\pm 0.5\text{ K}$. The software package WVASE32 was used for analysis [35]. The experimental errors caused by the window can be removed during the analysis. The surface morphology and ferroelectric domain texture of ANLT ceramics were imaged by atomic force microscopy and piezoresponse force microscopy (Dimension Icon, Bruker) with a conductive probe in the contact mode.

III. RESULTS AND DISCUSSION

Figure 1 displays the XRD pattern of ANLT ceramics at room temperature, indicating their typical perovskite structures. With increasing the LiTaO_3 composition, the diffraction peak variations shown in Figs. 1(b) and 1(c) illustrate that ANLT changes from AFE orthorhombic phase (JCPDS No.70-4738) to FE rhombohedral phase (JCPDS No.53-0346). Significantly, there is a mixed phase in ANLT05 ceramics, according to the appearance of both the characteristic peaks of AFE and FE phases, as shown in Fig. 1(d).

To explore more lattice details with LiTaO_3 composition, the structure variation for ANLT by summarizing IR-active and Raman-active phonon kinetics was implemented. Group theory predicts the molecule-vibrational modes in each phase of ANLT lattice. The zone-center (Γ -point) optical phonon

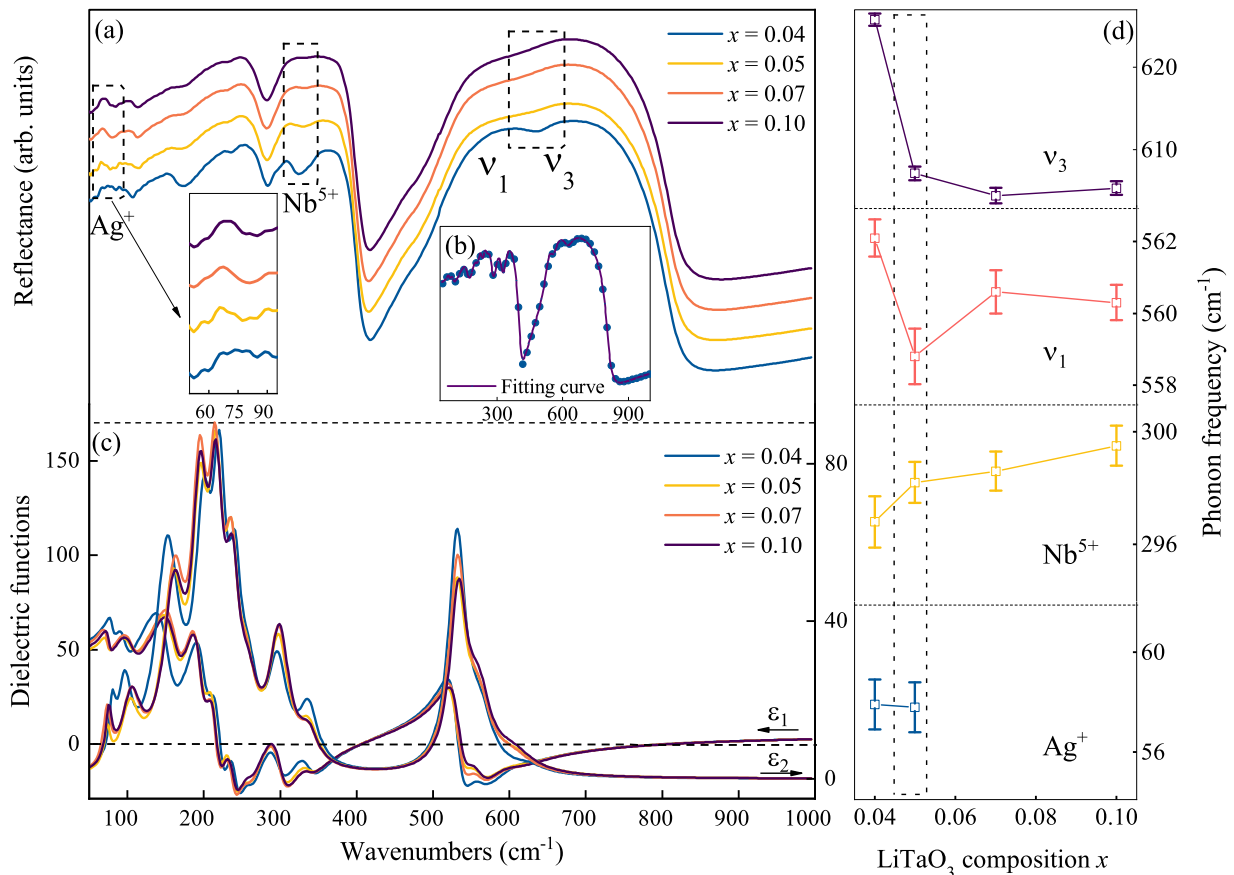


FIG. 2. (a) IR spectra of ANLT ceramics. The inset shows the enlarged frequency range of 50–90 cm⁻¹. (b) The experimental (point) and the best fitting (line) spectra of ANLT04 ceramics. (c) Real (ϵ_1) and imaginary (ϵ_2) parts of the dielectric functions obtained by fitting multiple Lorentz oscillators. (d) Frequency variation of four main phonon modes with increasing the LiTaO₃ composition at 300 K. The dashed boxes indicate the frequency variation anomaly.

modes of the $Pbcm$ [36,37] (M_1 phase) and the $R3c$ [37,38] (R phase) can be generalized as the following irreducible expressions, respectively:

$$\Gamma_{Pbcm} = 28A_1(\text{IR}) + 28A_2(\text{Raman}) + 32B_1(\text{IR}) + 32B_2(\text{Raman}), \quad (1)$$

$$\Gamma_{R3c} = 4A_1(\text{Raman, IR}) + 5A_2(-) + 9E(\text{Raman, IR}), \quad (2)$$

where all nondegenerated modes are labeled as IR- or Raman-active. Figure 2(a) displays IR reflection spectra of ANLT ceramics at room temperature. IR-active modes at high frequency (>350 cm⁻¹) and low range (<120 cm⁻¹) correspond to vibrations from the oxygen and A-site ions, respectively. The intermediate frequency range (120–350 cm⁻¹) is mainly associated with vibrations of Nb(Ta)-O bonds [39]. With the LiTaO₃ composition increases, the reflection peaks near 320 cm⁻¹ and 635 cm⁻¹ gradually disappear. The similar phenomenon of peak annihilation could be observed at 635 cm⁻¹ from pure AgNbO₃ during the thermal process [36]. For the doping composition of less than 0.05, multiple weak peaks appear at the frequency region of 50–100 cm⁻¹, as shown in the inset of Fig. 2(a). These peaks located at 50–100 cm⁻¹ gradually weaken with the LiTaO₃ composition, and finally become submerged. The phenomenon of peak annihilation

was also observed in the composition-dependent XRD results. It would be reasonably concluded that Li⁺ and Ta⁵⁺ are partially substituted on the sites of AgNbO₃ lattice, where Li⁺ replaces Ag⁺ at the A-site, and Ta⁵⁺ at the B-site, according to the ionic radii of Ag⁺ (1.28 Å), Li⁺ (0.92 Å), Nb⁵⁺ (0.64 Å), and Ta⁵⁺ (0.64 Å) ions. The doping of Li⁺ makes Ag⁺ deviate from the center of the oxygen octahedron, which leads to symmetry breaking and improves the degree of ordering. Therefore, the composition-dependent IR spectra reveal the lattice variations and phase transformation with the ionic substitution. The annihilation of the observed phonon modes located at 50–100 cm⁻¹ and near 320 and 635 cm⁻¹ would be a sign of the transition from M_1 to R phase, corresponding to the transformation from AFE to FE phase.

To further extract IR-active phonon frequency and summarize the infrared dielectric functions, IR spectra could be well fitted as shown in Fig. 2(b) by the multi-Lorentz oscillator model, following $\epsilon = \epsilon_1 + i\epsilon_2 = \epsilon_\infty + \sum_{n=1}^j \frac{A_j}{E_n^2 - E_n^2 + ib_r E_n}$, where ϵ_∞ refers to the contribution on the real part of complex dielectric functions, A is the amplitude, b_r is the damping coefficient, E_n represents the energy, and j represents the number of oscillators, respectively. The IR dielectric functions can be obtained by fitting the reflection spectra with Fresnel formula [40]: $\text{Rel} = \left| \frac{\sqrt{\epsilon} - 1}{\sqrt{\epsilon} + 1} \right|^2$. The real (ϵ_1) and imaginary (ϵ_2)

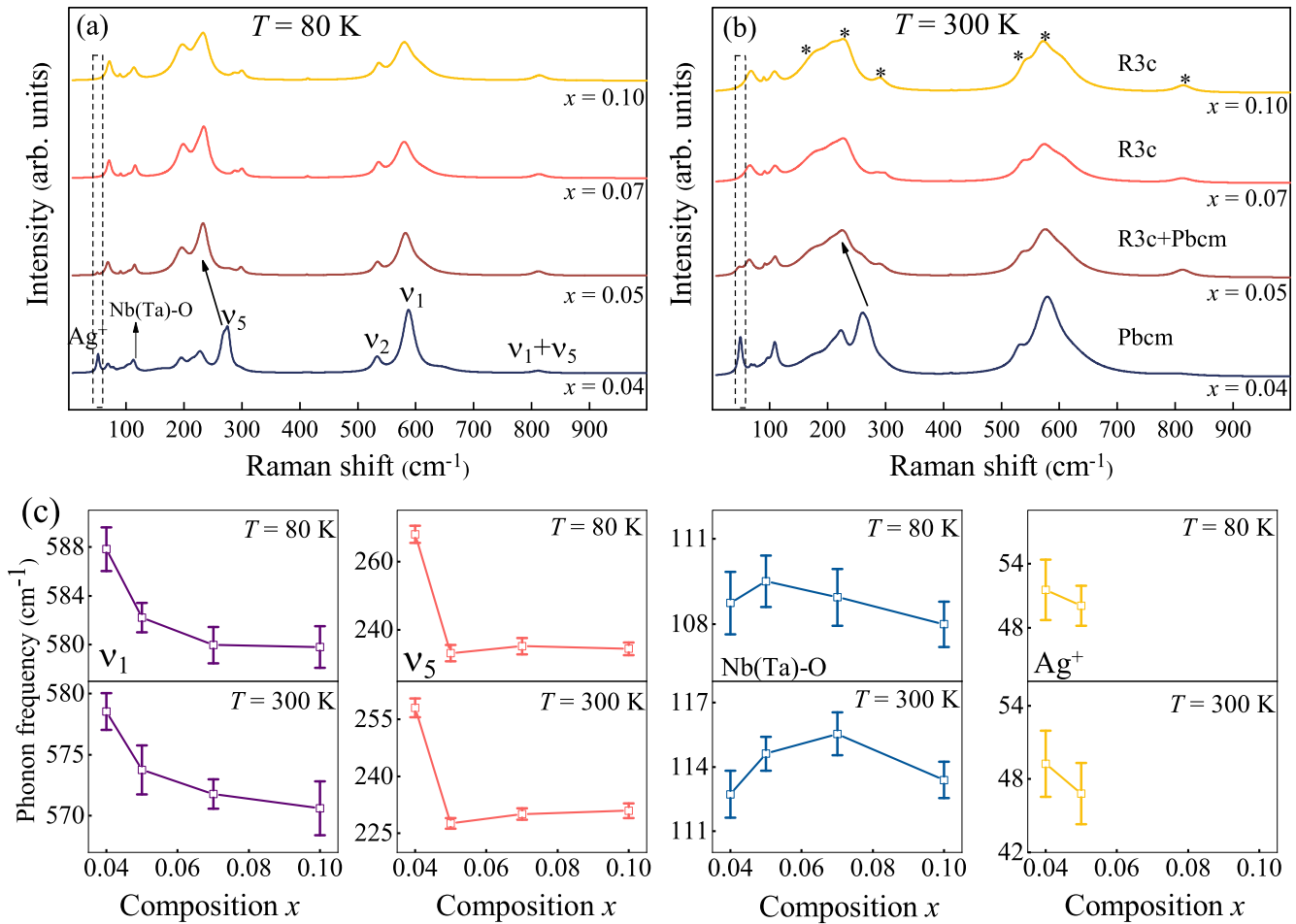


FIG. 3. Raman spectra of ANLT ceramics with different compositions at (a) 80 K and (b) 300 K, respectively. The dashed boxes indicate the obvious phonon anomaly. (c) The frequency trends of the main phonon mode with increasing the LiTaO_3 composition at 80 K and 300 K, respectively. Note that characteristic vibrational modes of the $R3c$ phase are assigned by (*).

parts of the dielectric functions are depicted in Fig. 2(c). It is difficult to identify all phonon behaviors due to the possibility of weak IR signals or peak overlap. IR spectra have been generally fitted by 12 oscillators, while phonon frequency of the weak IR modes in the low wave-number region is directly recognized from the spectra. For the frequency region of 650–1000 cm^{-1} , the ϵ_1 value gradually increases, while the ϵ_2 value is close to zero. It demonstrates that ANLT ceramics tend to be transparent at the frequency range of 650–1000 cm^{-1} .

Then, the frequency evolution of the main IR-active phonon with increasing the LiTaO_3 composition are depicted in Fig. 2(d). The modes around 620 and 560 cm^{-1} belong to the octahedral vibrations, which are primarily driven by the motion of the equatorial oxygen atom of the octahedron. Since Li^+ ions with the decreased sized replace Ag^+ sites, the octahedral dimension would shrink slightly, leading to changes in the tilt angle of the lattice and the symmetric stretching stress. Comparing the variations of the main phonon modes between ANLT04 and ANLT05, an obvious phonon softening process of A_{1g} (ν_1) and F_{1u} (ν_5) modes is related to the M_1 to R phase transitions. This structural transformation produces a strong ferroelectricity with respect to pure AgNbO_3 compound, which can be clearly comprehended from the un-

locking of strong local polarization due to the addition of LiTaO_3 [16]. Besides, peaks around 50 and 300 cm^{-1} are mainly derived from the breathing modes of Ag^+ and Nb^{5+} ions. The Ag^+ cationic vibration around 50 cm^{-1} could be collected clearly from ANLT04 and ANLT05 ceramics, while not existing in ANLT07 and ANLT10 ceramics. Therefore, considering the phonon behavior of ANLT05 ceramic, it suggests that its lattice structure can cross the transformation of AFE-FE phase, and be located at a two-phase-coexistence state for ANLT05 ceramic.

Raman spectra of ANLT ceramics at 80 K and 300 K are displayed in Figs. 3(a) and 3(b), respectively. The relatively strong peaks near 250 cm^{-1} and 600 cm^{-1} are assigned to the F_{2g} (ν_5) and ν_1 phonon modes, representing the main oxygen octahedral symmetry of ANLT lattice [41]. The spectra at the range of 50–300 cm^{-1} show the multiple peaks, which is from the translational modes of A-site cations (Ag^+ and Li^+) and the octahedral vibration of ν_5 [26,42]. The peak near 820 cm^{-1} can be affected by the vibrational coupling of ν_1 and ν_5 modes. The vibrations of Nb(Ta)-O bonds are observed at the frequency of 110 cm^{-1} . Characteristic vibrational modes of $R3c$ symmetry are denoted in Fig. 3(b), demonstrating the R phase at the doping compositions of above 0.05 [43]. As shown in Fig. 3(c), the composition-dependent frequency of

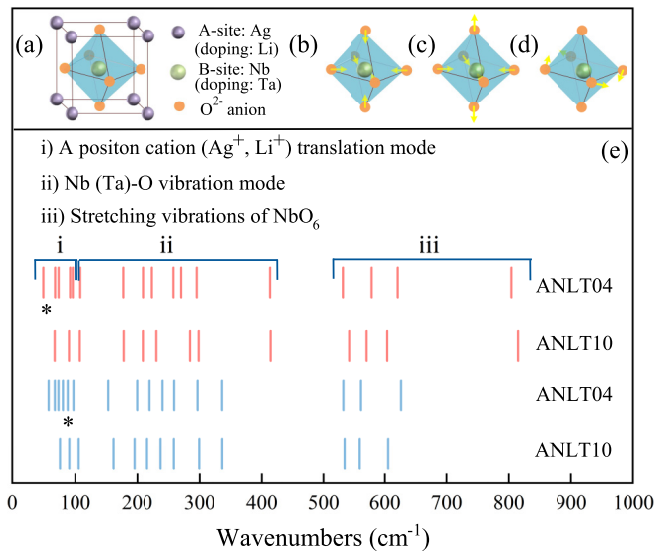


FIG. 4. (a) Schematic diagrams of the pseudolattice structure of AgNbO_3 doped with LiTaO_3 , and its main internal vibrating oxygen octahedron: (b) the stretched ν_1 mode, (c) the stretched E_g (ν_2) mode, and (d) the bending ν_5 mode. (e) A comparison of Raman-active and IR-active vibration modes for ANLT04 and ANLT10 ceramics. Redline is Raman-active mode, while the blue line is IR-active mode.

main vibration modes has been illustrated. Phonon modes of ν_1 and ν_5 obviously soften as the composition increases, whose trend is similar with those from IR-active modes. The frequency of the ν_5 mode in ANLT05 presents an enormous redshift from about 270 to 230 cm^{-1} with the heavier doping of Li^+ [44]. The oxygen octahedron is compressed under chemical pressure, leading to the decreased correlation length of displacements and polarizability. Simultaneously, the vibration of Nb(Ta)-O bonds becomes weakly sensitive to LiTaO_3 composition, owing to the similar ionic radius between Nb^{5+} and Ta^{5+} . The breathing mode of Ag^+ near 50 cm^{-1} could be only observed in ANLT04 and ANLT05, being consistent with IR spectra. In general, the appearance and suppression of Raman-active phonon are associated to structural modulation or the transformation of AFE-FE or FE-FE [45]. Therefore, comparing the composition dependence of the various Raman-active vibration modes, the different symmetry groups among the ceramics and AFE-FE phase boundary in ANLT05 could be confirmed at room temperature.

The schematic diagrams in Figs. 4(a) to 4(d) visualize the structure of basic lattice in the pseudocubic lattice, the stretching ν_1 , stretching E_g (ν_2), bending ν_5 modes, respectively. For comparison, Raman- and IR-active modes with the proposed assignments are summarized in Fig. 4(e). It can be seen that the numbers of the observed vibrational modes for ANLT04 ($Pbcm$) are more than those for ANLT10 ($R3c$), which phonon behavior is sensitive to structural change with the compositional doping. It is well known that the antiparallel displacement of Ag and Nb atoms along the b axis would contribute to AFE behavior. As the LiTaO_3 composition increases, the off-centered displacement of Li^+ is dominant and gives rise to the displacement of Ag^+ along the same direction, resulting in spontaneous polarization and the deriv-

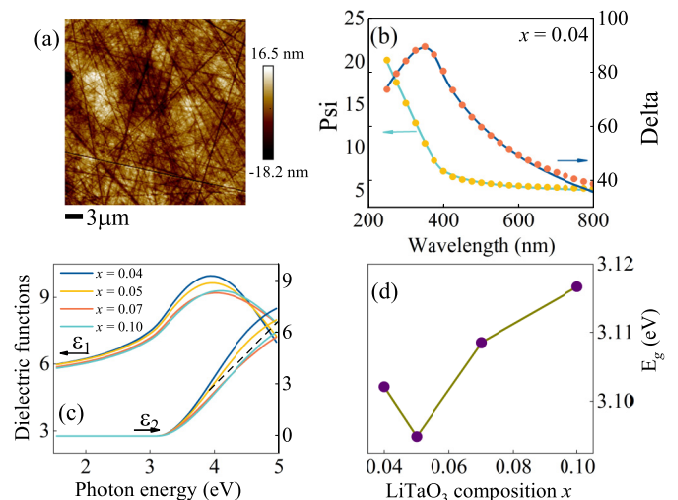


FIG. 5. (a) AFM topography of ANLT05 ceramic. (b) The experimental ellipsometric (dots) and the best-fitting (solid lines) spectra Ψ (Ψ) and Δ (Δ) of ANLT04 at 300 K. (c) The dielectric functions (ϵ_1 and ϵ_2) of ANLT ceramics. (d) The optical band gap (E_g) as a function of the LiTaO_3 composition x .

ing ferroelectricity. The lattice parameters present abnormal transition with the LiTaO_3 composition [23], which cannot be explained by the difference of ionic radius. It is related to the rotation of the octahedron, and the interrelationship between the two lattice structures. In addition, the change of octahedral rotation in LiTaO_3 -doped AgNbO_3 has been observed by neutron powder diffraction [46]. Upon LiTaO_3 substitution, the $a^0 a^0 c^+ / a^0 a^0 c^-$ configuration related to in-phase or antiphase octahedral tilting around [001] gradually becomes destabilized. The structural destabilization would become the driving force behind the composition-driven phase transition between the M_1 and R phases. Furthermore, in the process of AFE-FE structural transformation, the cationic breathing mode gradually disappeared. Overall, the composition-dependent phonon behavior unambiguously demonstrates that ANLT undergoes phase transitions from M_1 phase to the coexistence of the M_1 and R phases, then to the R phase with increasing LiTaO_3 composition. The coexistence of M_1 and R appears for ANLT05 at room temperature, which has a low energy barrier for polarization rotation [47], improving the pyroelectric, and energy-storage characteristics.

The exploration of optical transitions is important in reflecting intrinsic structure properties of ANLT. SE measurements can obtain dielectric functions ($\epsilon = \epsilon_1 + \epsilon_2$) by the relative change of the amplitude (Ψ) and phase (Δ) of polarized light in a particular direction. First, a rough layer exists on ANLT surface with the roughness of about 8.5 nm, as shown in the surface morphology image in Fig. 5(a). A three-layer structure model consisting of air, rough layer, and ANLT was built to fit the spectra. Besides, the rough layer was expressed by the Bruggeman effective medium model with air and ANLT accounting for 50%. For ANLT, the Tauc-Lorentz (TL) model was used, which can comply with the Kramers-Kronig constraints. A satisfactory fitting result was obtained, as evidenced by the good matching between experimental and simulation spectra shown in Fig. 5(b). The

TABLE I. The best-fitting parameters in the Tauc-Lorentz oscillator for SE at room temperature. Note that the error bars are also listed.

Sample	ε_∞	E_g (eV)	C	E_n (eV)	A	Roughness (nm)
$x = 0.04$	1.54 ± 0.15	3.10 ± 0.02	4.04 ± 0.24	4.36 ± 0.11	260.8 ± 4.5	12.32 ± 0.05
$x = 0.05$	1.59 ± 0.17	3.09 ± 0.02	4.57 ± 0.31	4.40 ± 0.11	258.2 ± 5.9	10.45 ± 0.04
$x = 0.07$	0.78 ± 0.20	3.11 ± 0.02	7.31 ± 0.54	4.42 ± 0.22	343.7 ± 5.2	9.35 ± 0.05
$x = 0.10$	1.14 ± 0.22	3.12 ± 0.02	5.77 ± 0.49	4.76 ± 0.11	263.2 ± 7.6	10.66 ± 0.05

best-fitting parameters of ANLT are listed in Table I. The expression of the TL model is given by [48] $\varepsilon_1(E) = \varepsilon_\infty + \frac{\pi}{\pi} P \int_{E_g}^{\infty} \frac{\xi \pi \varepsilon_2(\xi)}{\xi^2 - E^2} d\xi$, $\varepsilon_2(E) = \frac{AE_n C(E - E_g)^2}{(E^2 - E_n^2)^2 + C^2 E^2} \frac{1}{E} (E \geq E_g)$, $\varepsilon_2(E) = 0 (E < E_g)$, where P refers to the Cauchy principal part of the integral, ε_∞ is the high-frequency dielectric constant, and E is the incident photon energy. The parameters A , E_n , C , and E_g are the amplitude, peak position energy, broadening term, and optical band gap, respectively.

The optical dielectric functions with photon energy are depicted in Fig. 5(c). It demonstrates that the imaginary part ε_2 of all ANLT ceramics is zero below the absorption edge, indicating no electronic transitions at the low energy region. As the energy goes up, ε_2 suddenly increases because of strong absorption, indicating an interband electronic transition from the valence band maximum (VBM) to the conduction band minimum (CBM). The VBM of AgNbO_3 is constituted of the localized $\text{Ag } 4d$ and $\text{O } 2p$ orbitals along with the bonding orbital of $\text{O } 2p$ - $\text{Nb } 4d$, while the CBM mainly consists of the antibonding orbital of $\text{Nb } 4d$ - $\text{O } 2p$ [49]. The band structures of ANLT are closely associated with chemical bonding. The real part and imaginary parts of the dielectric functions present inconsistent trends between ANLT05 and ANLT07, which may be attributed to different lattice symmetries. Notably, the tilt of oxygen octahedron with the changed bond angle and length in the R phase is associated with the transition of band structure, which is collected in the spectra of dielectric functions. The parameter E_g experiences the trend of decreasing and then increasing with the composition growing, as displayed in Fig. 5(d). Upon the doping of the LiTaO_3 , the symmetry of the lattice structure decreases, resulting in the separation of the bonding orbital and the antibonding orbital (especially Nb-O) [49]. As the phase transition shifts to low symmetry, the degeneracy of these orbitals is lifted and the energy of crystal system is stabilized. However, E_g varies slightly with LiTaO_3 composition. It might be attributed to the extremely faint change of Nb-O bond length after LiTaO_3 doping, which is also figured out from composition-dependent Raman spectra.

To further reveal the spontaneous polarization properties of ferroelectric ANLT, the ferroelectric domain was explored by PFM. Rhombohedral ANLT ceramics allow 8 possible polarization vectors, formulating 71° , 90° , 109° , or 180°

domain configurations. Phase contrast indicates the different polarization directions of the domains. Antiparallel domain textures on ANLT05, ANLT07, and ANLT10 ceramics can be collected from the PFM phase channel in Figs. 6(a) to 6(c), respectively. In comparison, there are obvious differences of the domain size among them. The polarization distribution of ANLT05 presents the micrometer-sized striped domain, while that of ANLT07 performs smaller size on the nanoscale. Figures 6(d) and 6(e) show the nanoscale striped domain configuration with the size of a few hundred nanometers in ANLT10 ceramic, which holds the coexisted shape of micro and nanoscale domain in Fig. 6(c). Domain wall structure would be visualized in the PFM amplitude channel, where the piezoresponse would offset to a low magnitude at the domain wall. Surface-morphological interference could be eliminated, making the phase of PFM be not correlated to the sample morphology. In addition, because of the AFE behavior on the lattice scale, the ferroelectric domain of ANLT04 has not been observed by PFM, while the remaining three ceramics have clear striped-like domain structures. It would prove that the doped AgNbO_3 ceramics change from the AFE to FE phase with the LiTaO_3 composition.

Before the addition of LiTaO_3 , the off-centered cation and anion of AgNbO_3 move in opposite directions. The antiparallel displacement of the A site plays a key role in suppressing ferroelectricity and stabilizing the $Pbcm$ structure [50]. As the composition x increases, the displacement of the anion and cation tends to converge until a great change occurs at $x = 0.05$. This behavior may result from the reduced dipole moment in the sublattice, which contributes to the decrease of the $Pbcm$ symmetry and the appearance of the $R3c$ group. The competitive structural instability behind the component-dependent phase differences of AFE and FE may be caused by the combined contributions of the cationic antipolar and the octahedral tilt. A variety of evidences of the AFE and FE coexistence have been obtained, indicating its first-order phase transition.

Generally, AgNbO_3 -based ceramics undergo a successive phase transition of $M_1 \rightarrow M_2 \rightarrow M_3 \rightarrow O_1 \rightarrow O_2 \rightarrow T \rightarrow C$. However, there is still controversy about the existence of the O_2 phase [51,52]. ANLT05 has an excellent pyroelectric coefficient at room temperature, being comparable to lead-based materials. The temperature stability and phase transition process of ANLT are further considered. Temperature-dependent (80–800 K) Raman spectra are implemented to clarify the thermal evolution of phonon behavior for ANLT ceramics. According to fitting Raman spectra in Fig. 7(a) by multi-Lorentzian oscillator, Figures 7(b) to 7(e) summarize the temperature dependence of the phonon frequency for ANLT05, corresponding to modes of ν_1 , ν_5 , Nb(Ta)-O bonds, and Ag^+ , respectively. As the temperature increases at the range of 80–420 K, the frequency moves towards low wave-number range, caused by the anharmonic effect from thermal expansion of the lattice [53]. With heating to 420 K, the phonon frequencies of ν_1 , ν_5 , Nb(Ta)-O bond, and Ag^+ modes present anomalous shift, which could not be explained by the thermal effect. Similarly, the frequencies of the main vibration modes jump to a high wave number at temperature from 580 K to 680 K, while the frequency of ν_5 and the Nb(Ta)-O bond shifts abnormally at 680 K.

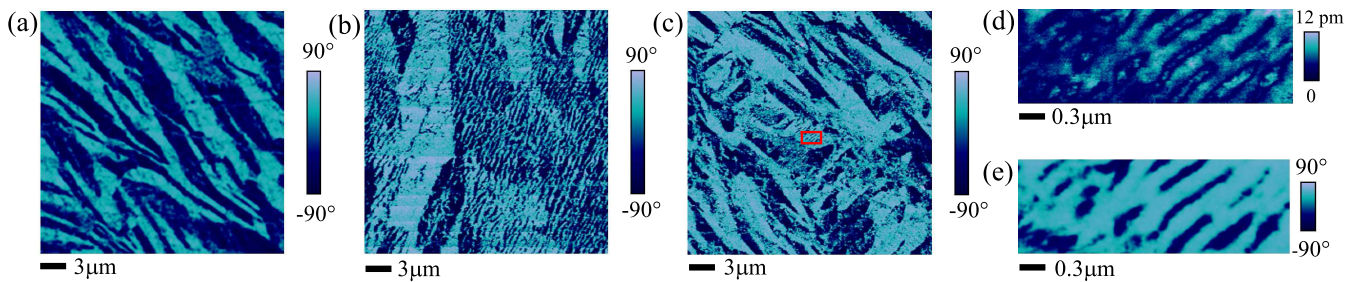


FIG. 6. PFM phase images for (a) ANLT05, (b) ANLT07, and (c) ANLT10 ceramics, respectively. The enlarged (d) amplitude and (e) phase image corresponding to the red box for ANLT10 ceramic.

During the heating process, the next anomalous shift occurs at 750 K. These abnormal frequency shifts reflect the thermally induced structural transition because phase transformation is accompanied by symmetric rearrangement and the redefinition of symmetric operation normally. Except for the inconsistency of the critical temperature among the samples, the lattice transformation ordering of ceramics is consistent with that of ANLT05, basically. In addition, the phonon mode around 50 cm^{-1} is recognized as a soft mode, being not observed in the rhombohedral phase [54]. The optical soft mode in $\text{Ag}(\text{Nb,Ta})\text{O}_3$ was first observed in IR and Raman spectra by Petzelt *et al.* [55]. They pointed out that the eigenvectors of both IR and Raman modes are active. The IR phonon mode remains active in the high-temperature phase, while the Raman phonon mode vanishes. In our paper, the soft mode with larger damping still remains Raman-active in *O* phase, while the soft mode does not generally exhibit Raman active in PE

phase. This phenomenon is reasonable because the *O* phase exists at a narrow temperature range and the thermal hysteresis of the lattice change due to the first-order phase transition characteristics. According to the temperature dependence of four main phonon, ANLT ceramics undergo a structural transformation from M_1 (*Pbcm*)/*R* (*R3c*) to M_2 (*Pbcm*) to M_3 (*Pbcm*) to *O* (*Cmcm*) to *T* (*P4/mbm*) phase as the temperature rises.

There is no evidence found for the existence of two intermediate orthorhombic (O_1 and O_2) structures over a narrow temperature range. The change of temperature may lead to the octahedral tilt, maintaining the optimal bonding of Ag^+ at the A site and Nb^{5+} at the B site. Structure transitions among *M* phases are related to the displacement of cations [13,44], while high-temperature phase transformations (*O*-*T* and *M*-*O*) are related to the octahedral tilt [12]. To clarify the details of the main phonon behavior and the critical temperature of ANLT ceramics at various phases, the observed frequencies of the typical phonon are summarized in Table II.

Finally, temperature-dependent (200–500 K) SE are used to investigate the thermal-induced optical transition behavior of ANLT ceramics. The values of dielectric functions for ANLT05 show a clear downward trend with the temperature from 200 to 430 K, while the peak for the real part of the dielectric function presents a redshift trend, as illustrated in Fig. 8(a). However, the abnormal phenomenon appears at over 440 K, which is associated with phase transition. Temperature-dependent E_g of ANLT05 in Fig. 8(b) demonstrates a redshift as temperature elevates from 200 to 430 K due to the temperature effect produced by the lattice expansion and the renormalization of the band structure [56]. E_g displays a skip shift at the temperature of 430–440 K differing from the thermal-induced redshift. The abnormal E_g shift might correspond to the M_1 - M_2 phase transition, which is related to the displacement of cations. The movement of the cation makes an influence on the orbital hybridization between the band structure of ANLT ceramics, further leading to the abnormal transitions of dielectric functions and E_g . Except for the transition temperatures, the thermal evolution of E_g and the dielectric functions for other ceramics are similar to those from ANLT05. It should be noted that the interband electronic transitions with the temperature are in a good agreement with the results from Raman spectra.

Overall, the phase diagram of ANLT ceramics with a composition temperature from Raman and SE spectra is

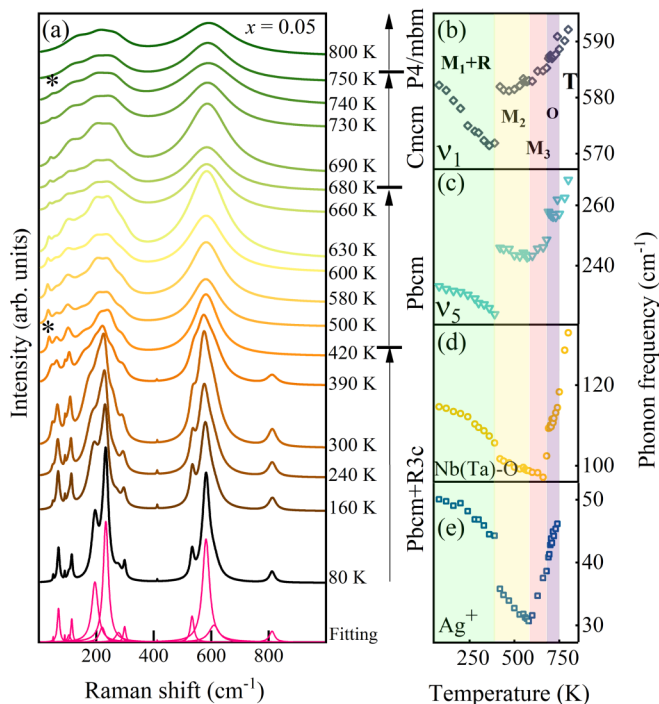


FIG. 7. (a) Temperature-dependent Raman spectra of ANLT05. Bottom shows the corresponding multi-Lorentz fitting process at 80 K. (b)–(e) Frequency evolution of main Raman-active phonon at 80–800 K for ANLT05 ceramic.

TABLE II. Center frequency of the main vibrational modes for R , M , O , and T phases in ANLT ceramics. The estimated error bars in each second line are achieved by considering the high-reliability fitting parameters and the lattice thermal expansion.

$x = 0.04$	Ag ⁺	Nb(Ta)-O	ν_1	ν_5	$x = 0.05$	Ag ⁺	Nb(Ta)-O	ν_1	ν_5
M_1	51.8	111	582.2	263	Intermediate phase	47.2	110.1	576.9	228.6
$Pbcm$	± 1.8	± 3.3	± 5.6	± 4.9	$Pbcm+R3c$	± 2.9	± 4.5	± 5.4	± 4.7
<320 K					<420 K				
M_2	42.4	105	578.7	258	M_2	33.3	100.3	582.7	244.4
$Pbcm$	± 5.6	± 2.6	± 2.5	± 3.1	$Pbcm$	± 2.6	± 1.5	± 0.7	± 1.4
320–510 K					420–600 K				
M_3	37.5	104.6	584	258.9	M_3	34.6	97.7	583.9	244.7
$Pbcm$	± 0.7	± 2.4	± 2.2	± 2.3	$Pbcm$	± 3	± 0.6	± 1	± 1.4
510–670 K					600–680 K				
O	39.9	109.6	587.1	258.2	O	42.4	108.4	589	259.8
$Cmcm$	± 0.3	± 0.9	± 0.3	± 0.5	$Cmcm$	± 3.8	± 6	± 2.5	± 2.5
670–710 K					680–750 K				
T	–	125.5	591	259.9	T	–	125.5	590.4	262.8
$P4/mbm$	–	± 4.2	± 2.2	± 2.4	$P4/mbm$	–	± 7.2	± 1.8	± 5.8
>710 K					>750 K				
$x = 0.07$	Ag ⁺	Nb(Ta)-O	ν_1	ν_5	$x = 0.10$	Ag ⁺	Nb(Ta)-O	ν_1	ν_5
R	–	111.3	574.3	230.7	R	–	108.5	574.6	231.3
$R3c$	–	± 5.2	± 5.7	± 4.5	$R3c$	–	± 5	± 5.2	± 3.1
<440 K					<490 K				
M_2	30.1	101	579.5	234.9	M_2	29.9	99.6	581.5	235.2
$Pbcm$	± 1.4	± 4.2	± 5.8	± 6.7	$Pbcm$	± 1.5	± 3.9	± 3.5	± 6.8
440–595 K					490–630 K				
M_3	33.9	100.5	585.4	241.5	M_3	31.7	99	586.9	238.9
$Pbcm$	± 4.1	± 2.5	± 1.2	± 1.8	$Pbcm$	± 2.5	± 1.3	± 1.9	± 1.4
595–720 K					630–770 K				
O	43.3	113.5	588.4	257.3	O	38.2	116.5	589.8	254.9
$Cmcm$	± 2.8	± 3.7	± 1.1	± 0.8	$Cmcm$	± 1.8	± 2.1	± 0.4	± 2.3
720–765 K					770–795 K				
T	–	126	592	263.3	T	–	120.5	590.8	257.7
$P4/mbm$	–	± 4.7	± 2.2	± 5.2	$P4/mbm$	–	± 0.5	± 0.2	± 0.9
>765 K					>795 K				

presented in Fig. 9. The doping of LiTaO₃ enhances the critical temperatures of M_2 - M_3 , M_3 - O , and O - T phase transitions, accompanying with the transitions among FE, AFE, and PE behaviors.

IV. CONCLUSION AND OUTLOOK

This work presents a systematical investigation on AgNbO₃ based ceramics, and clarifies the effect of the

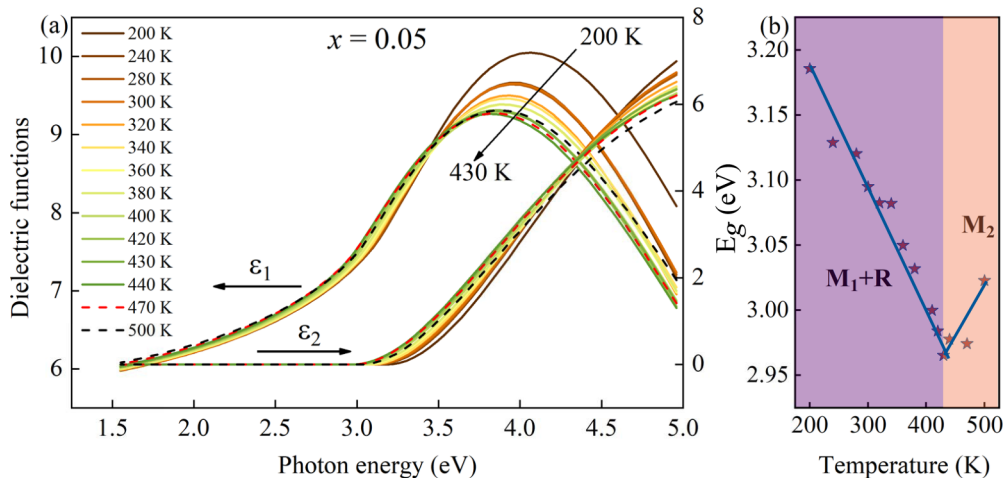


FIG. 8. (a) Dielectric functions for ANLT05 ceramics at different temperatures (200–500 K). (b) The optical band gap (E_g) is varied with respect to the temperature for ANLT05 ceramics.

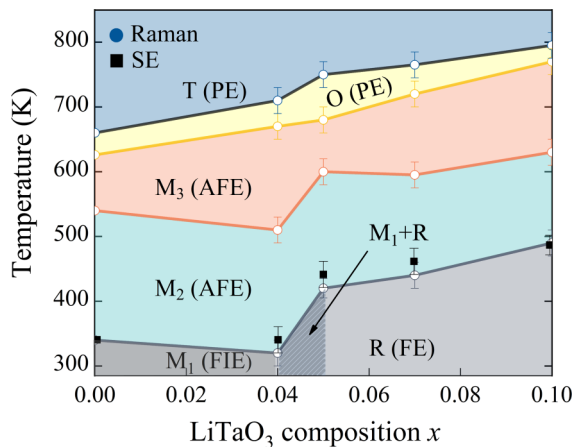


FIG. 9. LiTaO_3 compositions and temperature phase diagram of ANLT ceramics from Raman and SE data. The shaded area is the mixed phase of M_1 and R . The critical temperatures of pure AgNbO_3 are referred [11].

chemical doping by the optimized LiTaO_3 , in view of the lattice structure, molecular vibration, optical electronic transition, and domain behavior. We reveal the doping- and temperature-dependent behaviors of Raman/IR-active phonon, molecular symmetry, electronic transition, and structural phase transformation for AgNbO_3 ceramics, where dielectric functions and optical transition were explored through SE. Significantly, a mixed phase of AFE and FE is dramatically discovered for ANLT05 ceramics by XRD, IR,

and Raman spectra, indicating a first-order transition, actively contributing to the strengthened pyroelectric and energy storage performance. The phase transition of AFE to FE phase would be induced by a joint effect of the cationic antipolar and the oxygen octahedron distortion. A precise phase transition ordering (M_1/R - M_2 - M_3 - O - T) has been figured out by considering the consistent results of thermally induced phonon behaviors and E_g evolutions. Our research would improve the overall understanding of the phonon behavior, optical properties, domain structure, and structural transitions of high-performance AgNbO_3 ceramics, and promote development of AFE energy storage and pyroelectric materials and applications.

ACKNOWLEDGMENTS

This work was financially supported by the National Natural Science Foundation of China (Grants No. 91833303, No. 61805081, No. 61974043, No. 62074058, No. 62090013, No. 12104156, and No. 61974044), the National Key R&D Program of China (Grants No. 2019YFB2203403 and No. 2017YFA0303403), the Projects of Science and Technology Commission of Shanghai Municipality (Grants No. 18JC1412400, No. 18YF1407200, No. 18YF1407000, and No. 19511120100), China Postdoctoral Science Foundation (Grants No. 2020TQ0099 and No. 2020M681222), the Program for Professor of Special Appointment (Eastern Scholar) at Shanghai Institutions of Higher Learning and Shanghai Pujiang Program (20PJ1403600).

- [1] D. Zhang, W. Liu, R. Guo, K. Zhou, and H. Luo, *Sci. Adv.* **5**, 1700512 (2018).
- [2] N. H. Khansur, H. Kawashima, S. Wada, J. M. Hudspeth, and J. Daniels, *Acta Mater.* **98**, 182 (2015).
- [3] L. Yang, X. Kong, F. Li, H. Hao, Z. X. Cheng, H. X. Liu, J. F. Li, and S. J. Zhang, *Prog. Mater. Sci.* **102**, 72 (2019).
- [4] H. Tao, H. Wu, Y. Liu, Y. Zhang, J. Wu, F. Li, X. Lyu, C. Zhao, D. Xiao, J. Zhu, and S. J. Pennycook, *J. Am. Chem. Soc.* **141**, 13987 (2019).
- [5] H. Y. Xiao, W. Dong, Y. P. Guo, Y. F. Wang, H. Y. Zhong, Q. Li, and M. M. Yang, *Adv. Mater.* **31**, 1805802 (2019).
- [6] H. Moriwake, A. Konishi, T. Ogawa, C. A. J. Fisher, A. Kuwabara, K. Shitara, and D. Fu, *Phys. Rev. B* **97**, 224104 (2018).
- [7] Z. Liu, T. Lu, F. Xue, H. C. Nie, R. Withers, A. Studer, F. Kremer, N. Narayanan, X. L. Dong, D. H. Yu, L. Q. Chen, Y. Liu, and G. S. Wang, *Sci. Adv.* **6**, eaba0367 (2020).
- [8] Z. L. Lu, W. C. Bao, G. Wang, S. K. Sun, L. H. Li, J. L. Li, H. J. Yang, H. F. Ji, A. Feteira, D. J. Li, F. F. Xu, A. K. Kleppe, D. W. Wang, S. Y. Liu, and I. M. Reaney, *Nano Energy* **79**, 105423 (2021).
- [9] N. N. Luo, K. Han, M. J. Cabra, X. Z. Liao, S. J. Zhang, C. Z. Liao, G. Z. Zhang, X. Y. Chen, Q. Feng, J. F. Li, and Y. Z. Wei, *Nat. Commun.* **11**, 4824 (2020).
- [10] M. H. Francobe and G. Lewis, *Acta. Cryst.* **11**, 175 (1958).
- [11] P. Sciau, A. Kania, B. Dkhil, E. Suard, and A. Ratuszna, *J. Phys.: Condens. Matter* **16**, 2795 (2004).
- [12] I. Levin, V. Krayzman, J. C. Woicik, J. Karapetrova, T. Proffen, M. G. Tucker, and I. M. Reaney, *Phys. Rev. B* **79**, 104113 (2009).
- [13] I. Levin, J. C. Woicik, A. Llobet, M. G. Tucker, V. Krayzman, J. Pokorny, and I. M. Reaney, *Chem. Mater.* **22**, 4987 (2010).
- [14] D. Fu, M. Endo, H. Taniguchi, T. Taniyama, and M. Itoh, *Appl. Phys. Lett.* **90**, 252907 (2007).
- [15] D. Fu, M. Endo, H. Taniguchi, T. Taniyama, M. Itoh, and S. Koshihara, *J. Phys.: Condens. Matter* **23**, 075901 (2011).
- [16] D. Fu, M. Endo, H. Taniguchi, T. Taniyama, S. Koshihara, and M. Itoh, *Appl. Phys. Lett.* **92**, 172905 (2007).
- [17] D. Fu, M. Itoh, and S. Koshihara, *J. Appl. Phys.* **106**, 104104 (2009).
- [18] A. Kania, *J. Phys. D: Appl. Phys.* **34**, 1447 (2001).
- [19] A. Niewiadomski, A. Kania, G. E. Kugel, M. Hafid, and D. Sitko, *Mater. Res. Bull.* **65**, 123 (2015).
- [20] L. Zhao, Q. Liu, J. Gao, S. J. Zhang, and J. F. Li, *Adv. Mater.* **29**, 1701824 (2017).
- [21] M. Valant and D. Suvorov, *J. Am. Ceram. Soc.* **82**, 88 (1999).
- [22] M. Valant, D. Suvorov, C. Hoffmann, and H. Sommariva, *J. Am. Ceram. Soc.* **21**, 2647 (2001).
- [23] S. Li, H. C. Nie, G. S. Wang, N. T. Liu, M. X. Zhou, F. Cao, and X. L. Dong, *J. Mater. Chem. C* **7**, 4403 (2019).
- [24] M. Maczka, L. Macalik, and J. Hanuza, *J. Raman Spectrosc.* **40**, 2099 (2009).

- [25] H. C. Gupta, Archana, and V. Luthra, *Vib. Spectrosc.* **56**, 235 (2011).
- [26] A. Y. Cui, Y. Ye, L. M. Zheng, K. Jiang, L. Q. Zhu, L. Y. Shang, Y. W. Li, Z. G. Hu, and J. H. Chu, *Phys. Rev. B* **100**, 024102 (2019).
- [27] R. Singh, K. Kambale, A. Kulkarni, and C. Harendranath, *Mater. Chem. Phys.* **138**, 905 (2013).
- [28] Y. Ye, A. Y. Cui, M. Y. Bian, K. Jiang, L. Q. Zhu, J. Z. Zhang, L. Y. Shang, Y. W. Li, Z. G. Hu, and J. H. Chu, *Phys. Rev. B* **102**, 024103 (2020).
- [29] H. Qi, A. W. Xie, J. Fu, and R. Z. Zuo, *Acta Mater.* **208**, 116710 (2021).
- [30] Q. Q. Li, J. Y. Wang, M. J. Li, S. Guo, J. Z. Zhang, Z. G. Hu, Z. Y. Zhou, G. S. Wang, X. L. Dong, and J. H. Chu, *Phys. Rev. B* **96**, 024101 (2017).
- [31] J. Z. Zhang, W. Y. Tong, J. J. Zhu, J. Y. Xu, Z. H. Duan, L. P. Xu, Z. G. Hu, C. G. Duan, X. J. Meng, Z. Q. Zhu, and J. H. Chu, *Phys. Rev. B* **91**, 085201 (2015).
- [32] S. Kamba, *APL Mater.* **9**, 020704 (2021).
- [33] J. F. Scott, *Rev. Mod. Phys.* **46**, 83 (1974).
- [34] E. Buixaderas, I. Gregora, J. Hlinka, J. Dec, and T. Lukasiewicz, *Phase Transit.* **86**, 217 (2013).
- [35] J. A. Woollam, *Guide to Using WVASE32* (Lincoln, Lockport, NY, 2008).
- [36] J. Petzelt, S. Kamba, E. Buixaderas, V. Bovtun, Z. Zikmund, A. Kania, V. Koukal, J. Polivka, V. Pashkov, G. Komandin, and A. Volkov, *Ferroelectrics* **223**, 235 (1999).
- [37] D. L. Rousseau, R. P. Bauman, and S. P. S. Porto, *J. Raman Spectrosc.* **10**, 253 (1981).
- [38] Y. I. Yuzyuk, E. Gagarina, P. Simon, L. A. Reznichenko, L. Hennet, and D. Thiaudiere, *Phys. Rev. B* **69**, 144105 (2004).
- [39] K. G. Prasad, M. K. Niranjana, S. Asthana, and R. Karthikeyan, *J. Am. Ceram. Soc.* **99**, 332 (2016).
- [40] Z. H. Duan, P. Chang, Z. G. Hu, J. X. Wang, G. S. Wang, X. L. Dong, and J. H. Chu, *J. Appl. Phys.* **116**, 093513 (2014).
- [41] Y. H. Xu, Y. Guo, Q. Liu, Y. H. Yin, J. L. Bai, L. Lin, J. J. Tian, and Y. Tian, *J. Alloys Compd.* **821**, 153260 (2020).
- [42] X. Guo and N. Zhu, *J. Am. Ceram. Soc.* **90**, 2467 (2007).
- [43] U. Farid, H. U. Khan, M. Avdeev, T. A. Whittle, and B. J. Kennedy, *J. Solid. State. Chem.* **269**, 401 (2019).
- [44] H. U. Khan, I. Sterianou, S. Miao, J. Pokorny, and I. M. Reaney, *J. Appl. Phys.* **111**, 024107 (2012).
- [45] J. Pandey, D. Ghoshal, D. Dey, T. Gupta, A. Taraphder, N. Koratkar, and A. Soni, *Phys. Rev. B* **102**, 205308 (2020).
- [46] T. Lu, Y. Tian, A. Studer, N. Narayanan, Q. Li, R. Wither, L. Jin, Y. M. Gonzalez, A. P. Barranco, D. Yu, G. J. McIntyre, Z. Xu, X. Y. Wei, H. Yan, and Y. Liu, *Iucrj* **6**, 740 (2019).
- [47] W. F. Liu and X. B. Ren, *Phys. Rev. Lett.* **103**, 257602 (2009).
- [48] M. Z. Xie, M. Li, L. M. Li, J. Z. Zhang, K. Jiang, L. Y. Shang, Y. W. Li, Z. G. Hu, and J. H. Chu, *Appl. Phys. Lett.* **117**, 102101 (2020).
- [49] A. Shigemitsu and T. Wada, *Mol. Simulat.* **34**, 1105 (2008).
- [50] N. A. Benedek and C. J. Fennie, *J. Phys. Chem. C* **117**, 13339 (2013).
- [51] A. Ratuszna, J. Pawluk, and A. Kania, *Phase Transit.* **76**, 611 (2003).
- [52] U. Farid, A. S. Gibbs, and B. J. Kennedy, *Inorg. Chem.* **59**, 12595 (2020).
- [53] S. P. Pavunny, A. Kumar, and R. S. Katiyar, *J. Appl. Phys.* **107**, 013522 (2010).
- [54] M. D. Fontana, A. Ridah, G. E. Kugel, and C. C. Nedelec, *J. Phys. C: Solid State Phys.* **21**, 5853 (1988).
- [55] J. Petzelt, S. Kamba, and I. Gregora, *Phase Transit.* **63**, 107 (1997).
- [56] P. Lautenschlager, M. Garriga, L. Vina, and M. Cardona, *Phys. Rev. B* **36**, 4821 (1987).